Detection of Void in Karst Terrain with 3D Full Waveform Tomography

Khiem T. Tran, Ph.D.[1]; Michael McVay, Ph.D.[2]; Majid Mirzanejad[3]; and Scott Wasman, Ph.D.[4]

[1]Associate Professor, Univ. of Florida, Dept. of Civil and Coastal Engineering, 365 Weil Hall, PO Box 116580, Gainesville, FL 32611, U.S. E-mail: ttk@ufl.edu
[2]Professor, Univ. of Florida, Dept. of Civil and Coastal Engineering, 365 Weil Hall, PO Box 116580, Gainesville, FL 32611, U.S. E-mail: mcm@ce.ufl.edu
[3]Ph.D. Student, Univ. of Florida, Dept. of Civil and Coastal Engineering, 365 Weil Hall, PO Box 116580, Gainesville, FL 32611, U.S. E-mail: m.mirzanejad@ufl.edu
[4]Research Assistant Professor, Univ. of Florida, Dept. of Civil and Coastal Engineering, 365 Weil Hall, PO Box 116580, Gainesville, FL 32611, U.S. E-mail: scott.wasman@essie.ufl.edu

ABSTRACT

This paper presents a 3D surface-based full waveform inversion (FWI) method for detection of voids in karst terrain. The FWI method is based on a finite-difference solution of 3D elastic wave equations and Gauss-Newton inversion method. The key advantage of the waveform tomography approach is the ability to generate all possible wave propagation modes of seismic wavefields (body and surface waves) that are then compared with measured data to infer complex subsurface properties. Seismic wavefields are acquired from geophysical testing using sensors and sources located in uniform 2D grids on the ground surface, and then inverted for the extraction of 3D subsurface wave velocity structures. Field experiment was conducted at a karst site in Newberry, Florida, which is a dry retention pond, approximately 1.6 ha in size. The site has been susceptible to sinkhole formation with a number of open chimneys as well as large sinkholes that have formed and been repaired. Field experimental data were collected using 48 vertical receivers and a propelled energy generator (PEG, 40 kg model) on the ground surface to induce seismic wave energy. The 3D seismic inversion results show that the waveform analysis could be able to characterize the highly variable subsurface soil layers and karstic limestone bedrock at high resolution (meter pixel). An identified void was confirmed by SPT results.

INTRODUCTION

Full waveform tomography has become a popular geophysical tool for subsurface site characterization at various length scales from meters to kilometers. As documented by Vireux and Operto (2009), the full waveform tomography approach offers the potential to produce higher resolution models of the subsurface structures than approaches that consider only the dispersive characteristic of surface waves or first-arrival times of body waves. It can be used to identify and quantify embedded voids and characterize variable soil/rock layers, as the propagation properties of seismic waves are modulated by the voids and layer interfaces. Both shear wave and compression wave velocities (*Vs* and *Vp*) of subsurface structures can be determined independently to increase the credibility of characterized profiles.

2D FWI algorithms have been developed for detection of buried voids using refraction-type waveform data (Tran el al. 2013) and land-streamer waveform data (Tran and Sperry 2018). Results from experimental datasets have shown that full seismic surface wavefields provide useful information to locate buried voids. A void could be detected to a depth of 3 void diameters with surface measurements. However the 2D approach requires a test line placed on the top or in vicinity of a void for detectability, and thus multiple test lines are often needed to identify an unknown void. The 3D approach could potentially reduce field testing efforts, as waveform data are collected over an area instead of line by line.

A number of 3D FWI algorithms have been developed and applied to both synthetic and field seismic data at km-scales (Ben-Hadj-Ali et al. 2008; Epanomeritakis et al. 2008; Plessix 2009; Warner et al. 2013; Ha et al. 2015). Due to computational challenges for simulation of complete waveforms, the 3D FWI algorithms often use acoustic wave equations, therefore neglecting elastic effects. The acoustic approximation generally performs well for marine hydrophone data but is limited for land seismic data due to the importance of shear waves (Butzer et al. 2013), and thus cannot be used for geotechnical site investigation. Studies on elastic 3D FWI are still rare.

This paper presents a new 3D elastic FWI method for detection of buried voids. The method is based on 3D elastic wave equations for forward modeling to simulate wave propagation, and Gauss-Newton inversion approach for model updating to extract material property. The seismic wavefields obtained from 2D grids of sensors and sources on the ground surface are inverted to extract Vs and Vp structures.

METHODOLOGY

The presented 3D FWI method includes forward modeling to generate synthetic wave-fields, and an inversion to update model parameters. 3D elastic wave equations are used to simulate wave propagation, and Gauss-Newton method is used to minimize the residual between estimated waveform data obtained by forward simulation and observed seismic data for extraction of subsurface material properties.

Forward modeling of 3D wave propagation

For the forward modeling, 3D elastic wave propagation is described by a set of the first-order linear partial differential equations (using Einstein notation) for isotropic materials. The equation governing particle velocity in 3D is as follows:

$$\rho \dot{v}_i = \sigma_{ij,j} + f_i \tag{1}$$

The (constitutive) equations governing the stress-strain tensor are given as:

$$\rho \dot{\sigma}_{ij} = \lambda v_{k,k} + 2\mu v_{i,j} \quad \text{if } i = j \tag{2}$$

$$\rho \dot{\sigma}_{ij} = \mu(v_{i,j} + v_{j,i}) \quad \text{if } i \neq j \tag{3}$$

where σ_{ij} is the ij-th component of stress tensor (i, j =1, 2, 3), v_i is the particle velocity, f_i is the external force, ρ is the mass density and μ, λ are Lamé's coefficients of the material. The over dot (.) denotes the time derivative, and the comma (,) denotes the spatial derivative. For example, $v_{\mathrm{i,j}} = \dfrac{\partial v_i}{\partial x_j}$, or the spatial derivative with respect to x_j, which is the three spatial directions (x, y, z)

The classic velocity-stress staggered-grid finite difference method in the time domain (Virieux, 1986) i used to solve the equations. An accurate free-surface boundary condition is implemented by using the explicit finite difference and image technique (Robertsson, 1996) at the top boundary (ground surface), while the perfectly matched layer (PML) (Komatitsch and Martin, 2007) is applied at the other vertical and bottom boundaries.

Model updating by Gauss-Newton method

The Gauss-Newton method involves minimizing the residual between the estimated waveform data obtained by forward simulation and the observed seismic data from field testing. The residual is defined as:

$$\Delta \mathbf{d}_{s,r} = \mathbf{F}_{s,r}(\mathbf{m}) - \mathbf{d}_{s,r} \tag{4}$$

where indices *s* and *r* denote the *s*-th shot and *r*-th receiver, respectively, and the column vector $\mathbf{F}_{s,r}(\mathbf{m})$ is estimated waveform data associated with the model **m**, and obtained from the solution of the wave equations described by Equations 1- 3. Model **m** is a column vector consisting of *Vs* and *Vp* of all cells within a test domain. The column vector $\mathbf{d}_{s,r}$ is observed data for the *s*-th shot and *r*-th receiver. A set of observed data (column vector **d,** combined from all $\mathbf{d}_{s,r}$) includes signals from all shots and receivers. Both the shots and receivers are located in 2D uniform grids on the ground surface.

To minimize the residual, a least-squares error function E(**m**) is introduced as:

$$\mathrm{E}(\mathbf{m}) = \frac{1}{2} \| \Delta \mathbf{d} \|^2 = \frac{1}{2} \Delta \mathbf{d}^t \Delta \mathbf{d}, \; and \; \Delta \mathbf{d} = \{\Delta \mathbf{d}_{s,r}, s = 1..NS, r=1\ldots NR\}, \tag{5}$$

Where the superscript *t* denotes the matrix transpose, *NS* and *NR* are the numbers of shots and receivers, and Δ**d** is a column vector, which is the combination of residuals $\Delta\mathbf{d}_{s,r}$ for all shots and receivers. The size of Δ**d** is *NT* × *NS* × *NR,* where *NT* is the number of time steps. The updated model, $\mathbf{m}^{n+1}$, is obtained from Gauss-Newton approach for minimization of the error E(**m**) at the (*n+1*)-th iteration from the *n*-th iteration (Sheen et al. 2006) or:

$$\mathbf{m}^{n+1} = \mathbf{m}^n - \alpha^n [\mathbf{J}^t \mathbf{J} + \lambda_1 \mathbf{P}^t \mathbf{P} + \lambda_2 \mathbf{I}^t \mathbf{I} \;]^{-1} \mathbf{J}^t \Delta \mathbf{d}, \tag{6}$$

where **J** is the Jacobian matrix, or partial derivative wave-field with respect to individual model parameters (*Vs* and *Vp* of cells). The detailed calculation of matric **J** is presented in the following section. **I** is the identity matrix, and **P** is a matrix, whose elements are determined using a 3D Laplacian operator:

$$P_p \Delta \mathbf{m} = (\Delta m_p)^L + (\Delta m_p)^R + (\Delta m_p)^F + (\Delta m_p)^B + (\Delta m_p)^A + (\Delta m_p)^U - 6(\Delta m_p). \tag{7}$$

Where the superscripts *L*, *R*, *F*, *B, A* and *U* refer to six adjacent cells (left, right, front, back, above, and under) of the cell referring to the model parameter m_p, and P_p is the *p*-th row of the matrix **P** whose elements are either 1, -6, or 0. Coefficients λ_1 and λ_2 are constants, which are used for regularization and increase the invertability of approximate Hessian matrix (**$\mathbf{H_a} = \mathbf{J}^t\mathbf{J}$).** The choice of the coefficients from 0 to infinity is a compromise process. Larger values of λ_1 and λ_2 lead to smoother inverted models (not good for characterizing of material contrast), whereas smaller values produce more inversion artifacts. Several trial runs have been conducted in this study, and $\lambda_1 = 0.02$ and $\lambda_2 = 0.0005$ are selected. The step length α^n is close to 1.0 for the Gauss-Newton method, and it is fixed as 1.0 in this study.

FIELD EXPERIMENT AND RESULTS

The presented 3D FWI method was applied to field experimental dataset. Field experiment was conducted at a karst site in Newberry, Florida. The test site is a dry retention pond, approximately 1.6 ha in size. The site has been susceptible to sinkhole formation with a number of open chimneys as well as large sinkholes that have formed and been repaired. The site was divided into 25 north-south survey lines equally spaced a distance of 3.0 m apart. The lines were labeled A through Y from west to east across the site, with station 0 m located at the southern end of each line (Fig. 1a). The seismic survey was conducted at the northern portion of the site, where sinkhole activities were seen in the past.

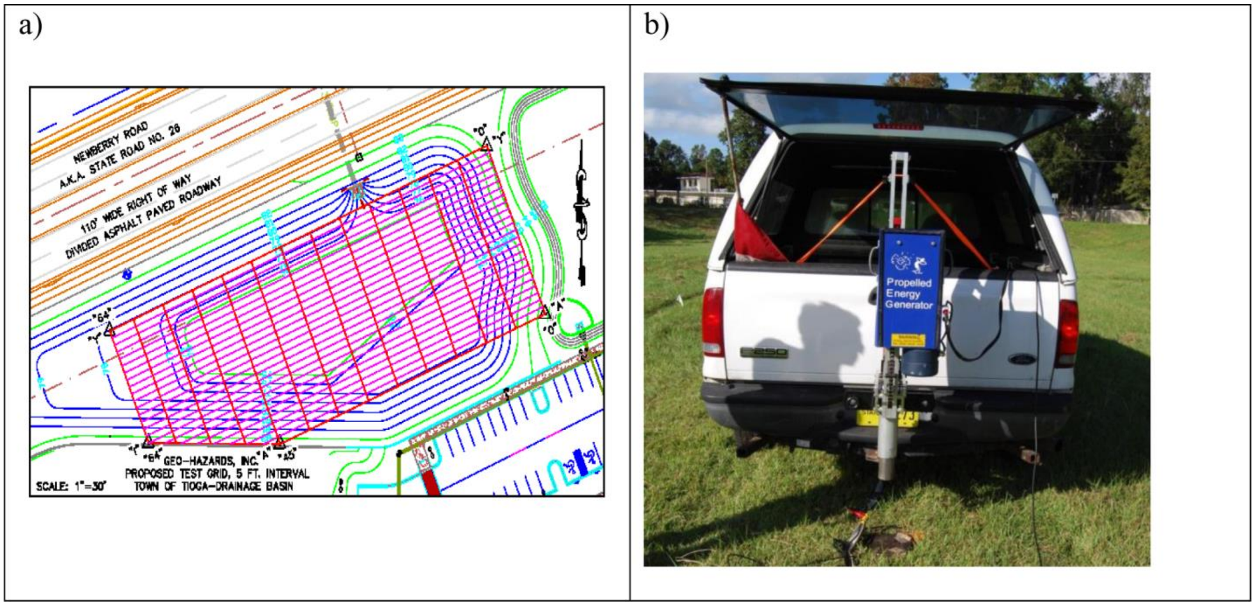

Figure 1. Field experiment: a) test site and b) propelled energy generator

The seismic wavefields were generated by a propelled energy generator (PEG, 40 kg model) as shown in Fig. 1b. The test area was at Lines O to R, using 2D grids of 48 receivers and 65 shots (Fig. 2). The receiver grid is 4 × 12 and source grid is 5 × 13, both at 3 m spacing. Generated wave-fields were simultaneously recorded by 24 4.5-Hz vertical geophones in two stages. In each stage, the 24 geophones were placed for a half of the receiver grid (2 × 12), and 65 shots were applied for the entire source grid (5 × 13). As the same impact load (same drop weight and height of the PEG) was applied at each shot location, the collected data from the two stages were simply combined to produce 48-channel shot gathers.

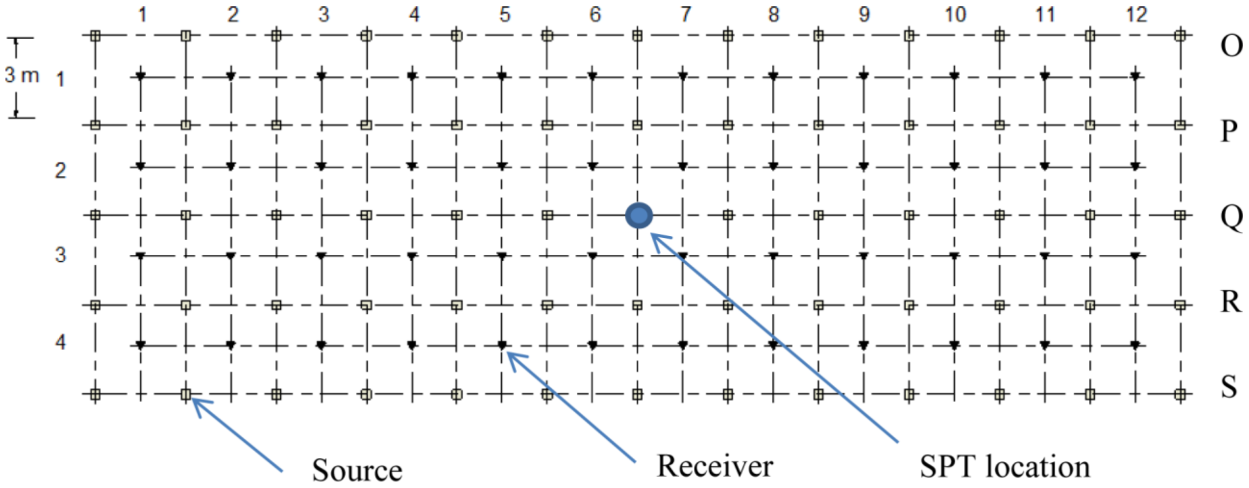

Figure 2. Field test configuration from Lines O to R: source (square), receiver (triangle). The standard penetation test (SPT) is at the center of seismic test area on Line Q.

Consulting the spectral analysis of measured data, the initial model (Fig. 3a) was established having *Vs* increasing with depth from 300 m/s at the surface (depth 0) to 600 m/s at the bottom of the model. The depth of model is taken as a half of the longer dimension of test area (or 18 m) to have good signal coverage for the analyzed domain. *Vp* was assumed twice of *Vs*. Two inversion runs were done for filtered data sets at two frequency bandwidths: 5 - 20 Hz and 5 - 30 Hz. The first run at 5 - 20 Hz began with the initial model, and the second run began with the inverted result of the first run.

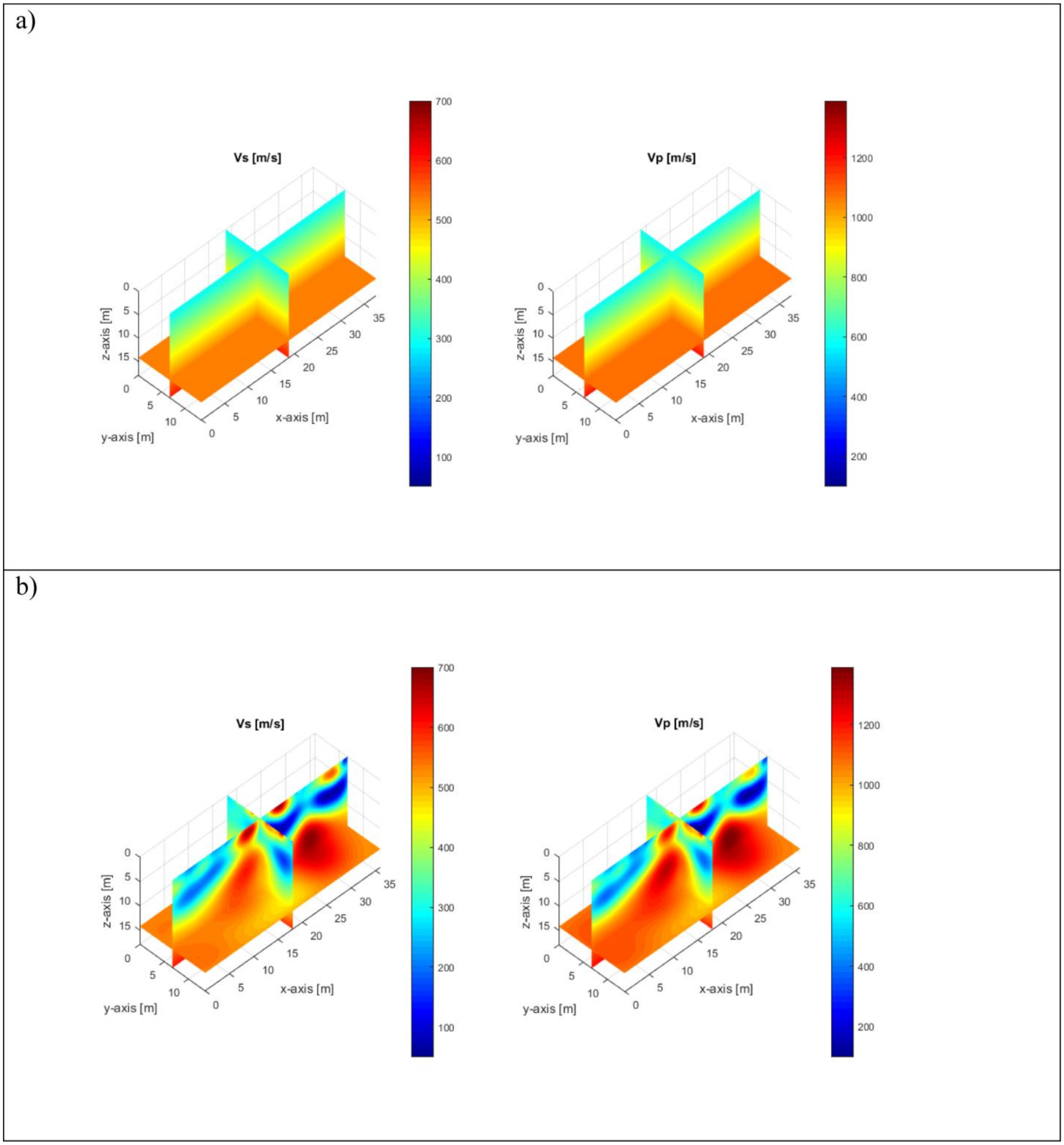

Figure 3. Field experiment: distribution of *Vs* and *Vp* (m/s): a) initial model used at the beginning of inversion; and b) final inverted models at 5-30 Hz.

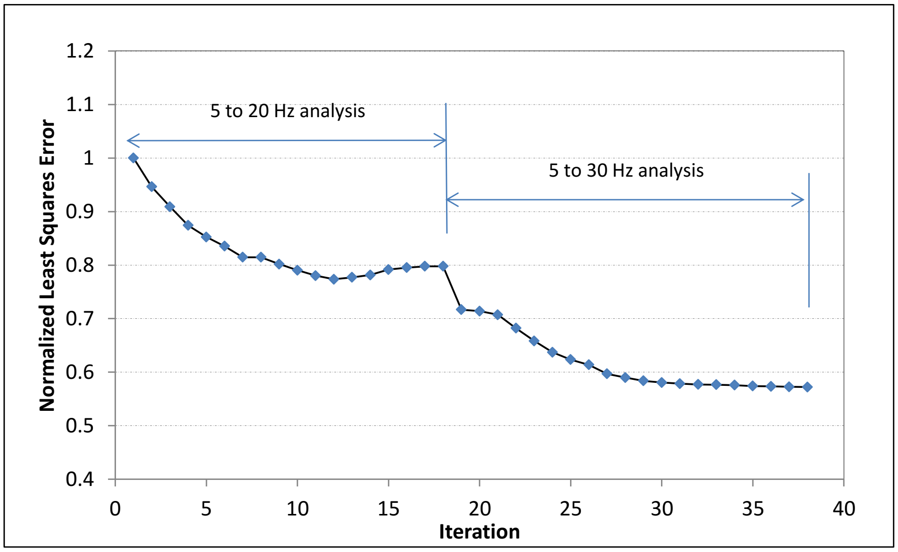

Figure 4. Field experiment: normalized least squares error versus the inversion iteration number for both inversion runs at 5-20 Hz and 5-30 Hz.

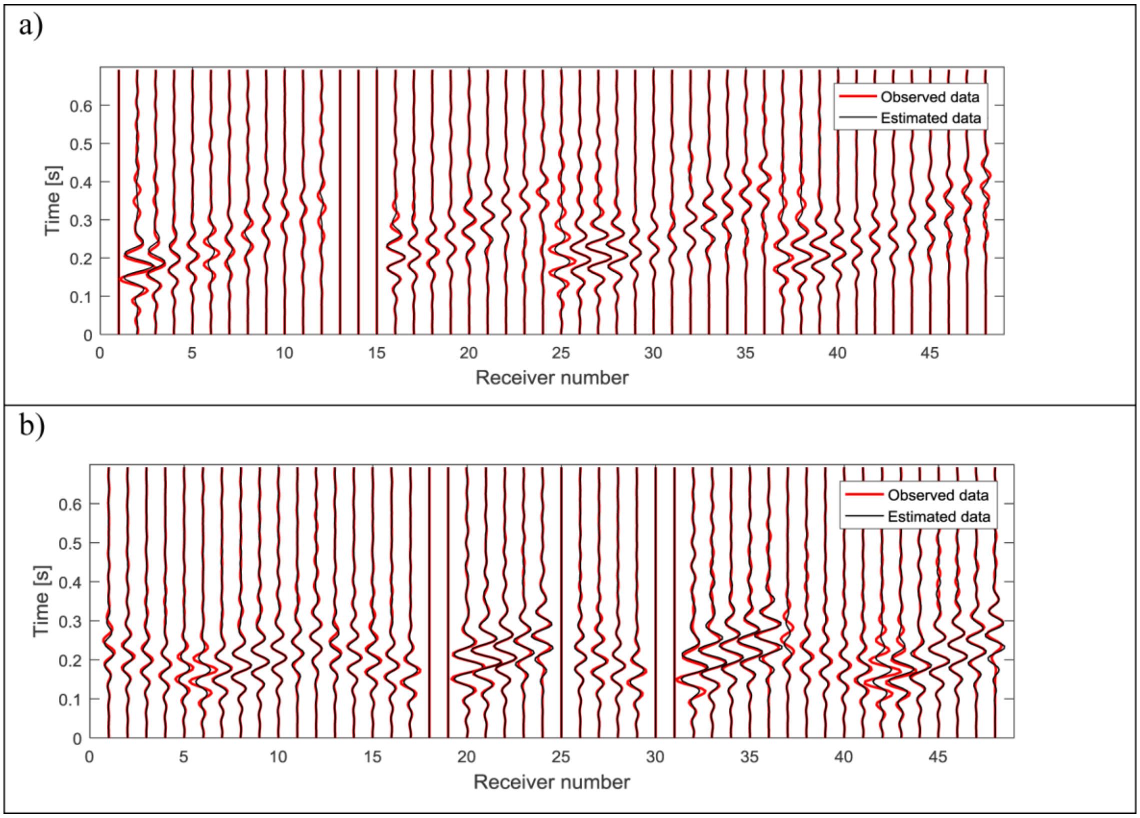

Figure 5. Waveform comparison for two sample shots: a) shot at a corner of test area, b) shot at the center of test area.

The 18 × 36 × 12 m (depth × length × width) medium was divided into 18,432 cells of 0.75 × 0.75 × 0.75 m. The cell size of 0.75 m was selected as a quarter of the geophone spacing (3 m), and used for both inversion runs. *Vs* and *Vp* of all cells were updated independently during inversion. The first and second inversion runs stopped at 17 and 21 iterations, respectively. The stopping criterion was set at the point when the least-squares error changed less than 1% from one to the next iteration for 3 consecutive iterations. The complete analysis took about 44 hours on a desktop computer (32 cores of 3.46 GHz each and 256 GB of memory).

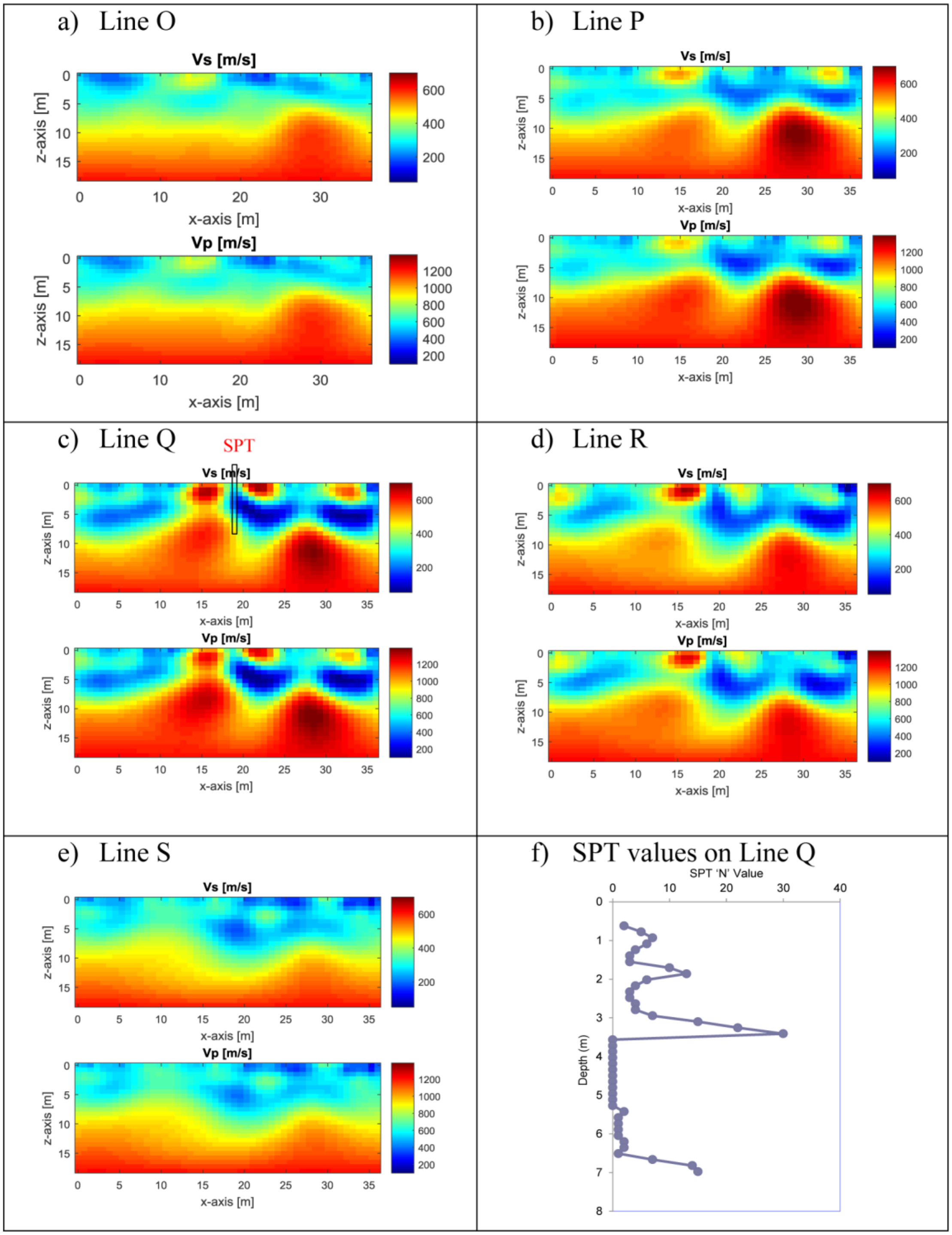

Figure 6. Field experiment: distribution of *Vs* and *Vp* along Lines O, P, Q, R, S, and SPT values.

Normalized least-squares error for all 38 iterations of the two inversion runs is shown in Fig.

4. The error reduces from 1.0 at the first iteration to about 0.57 at the final iteration, or 43% of the initial error was reduced during inversion. It is noted that the percentage of reduction depends the initial model. If the initial model is close to the true soil/rock profile (good initial waveform match), the error reduction is less, as it is more difficult to improve the waveform match. Fig. 5 shows the observed and estimated waveform data for all 48 receivers from two sample shots for the final iteration (iteration 38). Apparently, the observed and estimated waveform data match well for all channels. No cycle skiping is observed; suggesting the 1D initial model was sufficent.

The final inverted model for data at 5 - 30 Hz is shown in Fig. 3b. The *Vs* profile (Fig. 3b, top) consists of soft soil layers at shallow depths (0 ~ 5 m), underlain by a stiffer weather limestone layer (*Vs* ~ 600 m/s). Two shallow voids (*Vs* < 50 m/s) are identified at line Q. A few high-velocity zones are also imaged near the ground surface. These could be boulders or highly compacted soils from the past sinkhole repairs or simply be inversion artifacts at the source and receiver locations due to near-field effects or source/receiver cross-talk. The *Vp* profile (Fig. 3b, bottom) is consistent with the *Vs* profile.

For better reviewing lateral variation, Fig. 6 shows *Vs* and *Vp* profiles along lines O, P, Q, R, and S. Consistent variation of soil layers is observed along y direction. Also shown in Fig. 6 is the SPT location on line Q at x=18 m (center of test area), and the SPT ‘N’ values. The identified void at x = 18 m is confirmed at depth from about 4 to 7 m, where the SPT ‘N’ values are zeros (no materials). Verification of bedrock variation, the second void on line Q, and lateral dimensions of the voids are undergoing with more invasive tests.

CONCLUSION

A 3D FWI method is presented for detection of voids in karst terrain. The FWI method is based on a finite-difference solution of 3D elastic wave equations and Gauss-Newton inversion method. Seismic wavefields are acquired from geophysical testing using sensors and sources located in uniform 2D grids on the ground surface, and then inverted for the extraction of 3D subsurface wave velocity structures. The field results from a karstic test site in Florida show that the waveform analysis could be able to characterize the highly variable subsurface soil layers and limestone bedrock at high resolution (meter pixel). The identified void was confirmed by a SPT.

ACKNOWLEDGMENTS

This study was financially supported by the National Science Foundation: grant CMMI-1637557, and Florida Department of Transportation (FDOT): grant BDV31-977-82. The supports are greatly appreciated. The authors would like to thank the FDOT State Materials Office in Gainesville, FL for providing access to the test site and conducting the SPT data.

REFERENCES

Ben-Hadj-Ali, H., Operto S., and Virieux J. (2008). Velocity model building by 3D frequency-domain, full-waveform inversion of wide-aperture seismic data: *Geophysics*, 73 (5), VE101–VE117.

Butzer S., Kurzmann A. and Bohlen T. (2013), “3D elastic full-waveform inversion of small-scale heterogeneities in transmission geometry”, *Geophysical Prospecting,* 2013, 61, 1238–1251.

Epanomeritakis I., Akcelik V., Ghattas O. and Bielak J. (2008). A Newton-CG method for largescale three-dimensional elastic full waveform seismic inversion: *Inverse Problems* 24, 26 pp.

Ha W., Kang S., and Shin C. (2015). 3D Laplace-domain waveform inversion using a low-frequency time-domain modeling algorithm: *Geophysics*, 80(1), R1-R13.

Kamatitsch D. and Martin R. (2007). An unsplit convolutional perfectly matched layer improved at grazing incidence for the seismic wave equation: *Geophysics;* 72(5), SM155–SM167.

Plessix R. (2009). Three-dimensional frequency-domain full-waveform inversion with an iterative solver: *Geophysics,* 74:WCC149-WCC157.

Robertsson, J. O. A., (1996). A numerical free-surface condition for elastic/viscoelastic finite-difference modeling in the presence of topography, *Geophysics*, 61, 1921–1934.

Sheen D.H., Tuncay K., Baag C. E. and Ortoleva P. J. (2006). Time domain Gauss–Newton seismic waveform inversion in elastic media: *Geophysical Journal International,* 167: 1373-1384.

Tran K.T. and Sperry J. (2018). Application of 2-D Full Waveform Tomography on Land-streamer Data for Assessment of Roadway Subsidence, *Geophysics*, Vol. 83, (3), pp. EN1–EN11.

Tran K.T., McVay M., Horhota D., and Faraone M. (2013). Sinkhole Detection Using 2D Full Seismic Waveform Tomography, *Geophysics*, Vol. 78 (5), pp. R175–R183.

Virieux J. (1986). P–SV wave propagation in heterogeneous media: velocity–stress finite-difference method: *Geophysics*; 51(4): 889–901

Vireux J. and Operto S. (2009). An overview of full-waveform inversion in exploration geophysics: *Geophysics*; 74(6): WCC1-WCC26.

Warner M., Ratcliffe A., Nangoo T., Morgan J., Umpleby A., Shah N. (2013). Anisotropic 3D full-waveform inversion: *Geophysics,* 78(2), R59–R80.